



# Planar Front Growth of Single Crystal Ni-Based Superalloy René N515

SAE MATSUNAGA <sup>1,3</sup> DUO HUANG,<sup>1</sup> SAMUEL B. INMAN,<sup>1</sup>  
JACK C. MASON,<sup>1</sup> DOUG KONITZER,<sup>2</sup> DAVID R. JOHNSON,<sup>1</sup>  
and MICHAEL S. TITUS<sup>1</sup>

1.—School of Materials Engineering, Purdue University, West Lafayette, IN 47907, USA. 2.—GE Aviation, Evendale, OH 45215, USA. 3.—e-mail: smatsun@purdue.edu

A Ni-based superalloy, René N515, was fabricated by the levitation zone melting process to produce planar front single crystal growth. Microstructure, alloy composition, and microhardness properties of the as-zone melted and solution heat treated alloy were investigated and compared with the directionally solidified state to study the effect of microsegregation on these alloy characteristics. In the planar front region, the dendritic structure and microsegregation were eliminated, and the density of casting porosity decreased as well. We modeled the zone melting/planar growth process by solving the zone melting mass balance equation numerically, and the measured and predicted composition profile of the planar front were in good agreement. The Vickers microhardness did not vary throughout the planar front region. These results indicate that a nearly homogeneous planar front of a 2nd-generation single Ni-based superalloy can be fabricated via levitation zone melting, and common casting defects can be eliminated entirely.

## INTRODUCTION

Ni-based superalloys have been widely used for high-temperature applications such as turbine blades for jet propulsion and power generation plants due to their superior balance of properties at elevated temperature that include resistance to creep, fatigue, and oxidation.<sup>1</sup> These properties are in part obtained by the unique microstructure of Ni-based superalloys which is composed of a solid-solution disordered face-centered cubic  $\gamma$  matrix with coherently embedded  $\gamma'$  precipitates with a  $L1_2$ - $Pm\bar{3}m$  crystal structure.<sup>1</sup> The high pressure turbine blades in these turbine engines are exposed to corrosive environments at elevated temperature and are subjected to severe stresses resulting from centrifugal and aerodynamic forces.<sup>2</sup> These extreme operating conditions motivated the development of new materials that significantly improve the creep resistance of these alloys.

The advent of new materials and manufacturing methods culminated in the development of advanced directional solidification processes in the 1970 s, which included the Bridgman process that is able to produce “single crystal” turbine blades

containing virtually no grain boundaries.<sup>2</sup> In this method, a Ni-based superalloy charge is melted (via induction or convection heating) and then poured into an investment mold held at a temperature above the liquidus temperature of the alloy. The mold and superalloy are then withdrawn downward into vacuum or other coolant as shown in Fig. 1a. To maintain dendritic solidification, the mold and superalloy are withdrawn at a constant withdrawal rate and thermal gradient, as shown in the  $v$ - $G$  processing map in Fig. 1b. Maintaining a steady thermal gradient enables the growth of highly oriented [001] dendrites, which nearly eliminates grain boundaries in the single crystal. The absence of grain boundaries prevents the formation of voids and cavitation which are primary crack initiation sites during creep in equiaxed microstructures.<sup>3</sup> Additionally, the absence of grain boundaries allows for the removal of grain boundary strengthening elements in the alloy composition that form carbides and borides, which can serve as initiation sites in fatigue in Ni-based superalloys.<sup>4</sup>

In addition to new solidification processes, engine manufacturers have improved creep resistance by alloying with specific elements, particularly

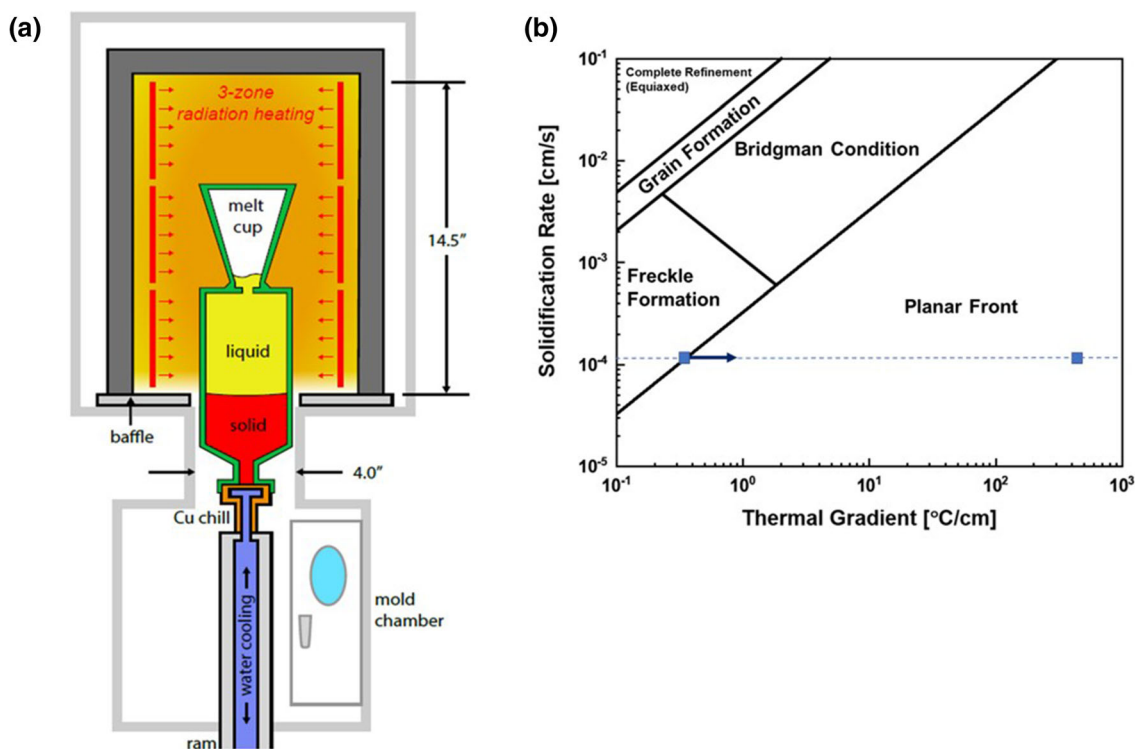


Fig. 1. Schematic images of (a) Bridgman casting process, and (b) the processing map of the directional solidification of single crystal Ni-based superalloys. (b) Was adapted from references<sup>7</sup> and<sup>24</sup> and the actual solidification rate for the levitation zone melting process was added using the dotted line and square symbol. The thermal gradient can be varied within the planar front region with a constant solidification rate.

refractory elements such as Ti, Nb, Ta, W, Hf, and Re.<sup>2</sup> Rhenium, in particular, is a potent alloying element that significantly improves the creep resistance of these alloys, though the exact mechanism is still not well understood.<sup>5</sup> Alloying of heavy elements can negatively influence the castability of superalloys due to a tendency for these alloying elements to create convective instabilities in the mushy zone (liquid + solid) and significant residual microsegregation. During directional solidification, microsegregation occurs due to non-equilibrium solidification and is observed as compositional inhomogeneity throughout the dendritic microstructure.<sup>2,6</sup> Microsegregation can cause the formation of low-melting temperature or brittle phases and a non-uniform distribution of  $\gamma'$  precipitates,<sup>7</sup> which are detrimental to mechanical properties.<sup>8</sup> Furthermore, because the dendrite growth direction is antiparallel to gravity in the Bridgman process, a density inversion can form between the liquid metal in the mushy zone and the liquid metal outside of the mushy zone. This inversion can initiate thermosolutal convection and cause the formation of the casting defects known as freckles.<sup>9</sup> Freckle chains are small chains of equiaxed grains oriented along the solidification direction and form due to highly enriched solute content in the liquid that suddenly freezes.<sup>10</sup> The compositions of these grains differ from the bulk composition; they are typically

enriched in the elements concentrated at the interdendritic region and may contain high angle grain boundaries that can act as crack initiation sites.<sup>1,9</sup>

Fabrication of a truly homogeneous microstructure free of secondary phases, grain boundaries, porosity, and microsegregation may then improve the mechanical and environmental properties of advanced Ni-based superalloys. Some work has been done to elucidate the creep and fatigue life credit afforded by eliminating casting defects.<sup>11–13</sup> This study has been conducted to understand the planar front solidification process of advanced Ni-based superalloys. In this study, a Ni-based superalloy was fabricated via planar front growth in order to explore the possibility of eliminating microsegregation and secondary phase formation. The composition, microstructure, and microhardness profiles will be presented. A thermodynamic model was developed to predict the as-solidified concentration and phase fraction profile. The results from experimental studies and modeling will be compared, and the influence of planar front microstructure to compositional and mechanical properties will be discussed.

## METHODOLOGY

A René N515 [Ni – 6.95 Cr – 7.87 Co – 1.29 Mo – 2.10 W – 14.43 Al – 2.22 Ta – 0.498 Re – 0.208 Hf – 0.206 C – 0.023 B (at.%)] directionally solidified bar, 15 mm in diameter and approximately 150 mm

long, was provided in the as-cast state by GE Aviation and used to fabricate a planar front grown bar. The as-cast bar was sectioned in half and fastened in a levitation zone melting furnace to top and bottom grips. Levitation zone melting<sup>14–16</sup> was carried out using a 25-mm single turn induction coil operating at 17 kW under an Ar-5%H<sub>2</sub> atmosphere; a schematic of the levitation zone melter is shown in Fig. 2.<sup>15</sup> The two ends of the bars were brought to within 5 mm of each other until the molten zone was formed. Once the top of the bottom bar started to melt, the top bar was translated downward to create a molten zone between the two bars. In levitation zone melting, the liquid is partially levitated between the upper and lower bars and provides for the processing of crystal diameters for which surface tension alone would be insufficient to contain the molten zone in a containerless environment.<sup>14</sup> The bottom bar, which is used to seed the crystal growth, consisted of a René N515 single crystal with a  $\langle 100 \rangle$  orientation. During processing, the bottom bar was rotated between 27 rpm and 124 rpm to average the power input from the induction coil and promote a flat solid–liquid interface.<sup>16</sup> Both bars were translated through the induction coil at a rate of 3 mm/h ( $8.3 \times 10^{-5}$  cm/s) to fabricate planar front grown single crystals (PG). The size of the molten zone was maintained at a diameter equal to that of the as-cast bars by moving the top bar relative to the bottom through stretch/squeeze control.<sup>17</sup> While the upper solid/liquid interface was melted, the bottom interface was frozen and a water-cooled radiation jacket surrounding the solidified bar promoted a high thermal gradient.

The planar growth bar was sectioned longitudinally using electrical discharge machining for both microstructural characterization and compositional analysis. One half of the sectioned material was additionally subjected to a solution anneal at 1313°C for 1 h. The microstructure characterization

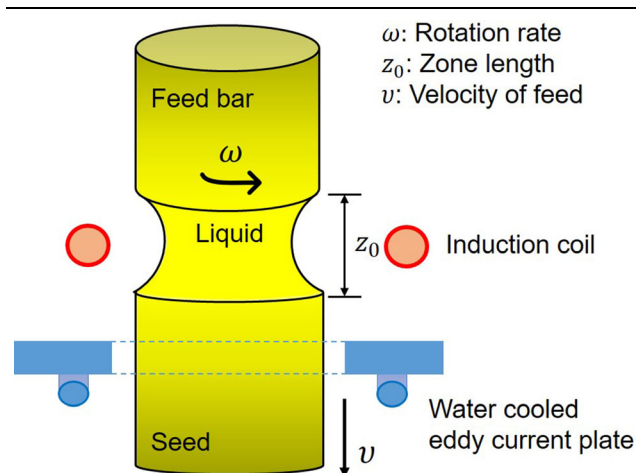


Fig. 2. Schematic image of levitation zone melting. Adapted from Ref.<sup>15</sup>.

for both the as-received, as-grown, and solution heat treated (SHT) samples was carried out using an FEI Quanta 650 and FEI Quanta 3D FEG scanning electron microscopes (SEM) with a backscatter electron detector. The specimens were mechanically ground using SiC paper to 2000 grit, polished from 6 μm to 1 μm with diamond paste, and vibratory polished for 2 h using 0.06 μm colloidal silica. Electron probe microanalysis (EPMA) was performed using a JEOL JXA8200 WD/ED Combined Microanalyzer Superprobe to investigate the segregation characteristics of the zone-melted sample before and after solution heat treatment. EPMA measurements were made over 16.75 mm at a step size of 50 μm. EPMA measurements shown here only include those from the SHT specimen. The as-grown and SHT specimens exhibited comparable composition profiles; however, the profile was less noisy in the SHT specimen due to the absence of coarsened γ' precipitates. Microhardness of the as-grown material was measured by Vickers microindentation using a Wilson® Tukon™ Vickers hardness tester. The indent was spaced every 200 μm with a load of 500 g. The measurements were repeated once.

The general solution to the zone melting equation for a binary system can be expressed as:

$$C_S(z) = C_0 \left( 1 - (1 - k_0) e^{-\frac{k_0 z}{z_0}} \right) \quad (1)$$

where  $z$  is the position along the bar,  $C_S$  is the composition of the solid,  $C_0$  is the initial composition,  $k_0$  is the partition coefficient, and  $z_0$  is the zone length. The differential form of this zone melting equation was coupled to a thermodynamic database (TCNI8) and TQ-Interface and numerically solved to predict solute concentration along the length of the bar.

To model the concentration profile of the planar front, the following assumptions were considered for simplicity: (1) the model is one-dimensional and does not consider composition variation in the radial direction, (2) the travel rate and liquid zone dimension is constant, (3) diffusion is infinitely fast in the liquid but negligible in solid. Algorithm 1 outlines the computational process of the model. The initial composition of the alloy  $C_0$ , zone length  $z_0$ , length of planar growth region  $L$ , system pressure  $P$ , and the step size  $dz$  were input as initial conditions. An initial phase equilibrium calculation was performed at the freezing liquid/solid interface while the liquid zone moved towards the bar end. As the liquid zone moved towards the end, a phase equilibrium calculation was performed for each step. The composition of the solid at distance  $z$ ,  $C_S(z)$ , was determined by the calculation and the corresponding liquid composition  $C_L(z + dz)$  for the next step was calculated by the following equation based on mass balance:

$$C_L(z) \cdot z_0 - C_S(z) \cdot dz + C_0 \cdot dz = C_L(z + dz) \cdot z_0 \quad (2)$$

The phase fractions were calculated at 1340°C, 1300°C, and 1100°C using the predicted solid composition profiles obtained from the zone melting model with the Thermo-Calc TCNI8 database.

## RESULTS

The as-received directionally solidified (DS) microstructure of René N515 is shown in Fig. 3. A typical dendritic structure with interdendritic regions and carbides was observed. The secondary dendrite arm spacing was in the range of 70–85  $\mu\text{m}$ . Carbides formed in the interdendritic regions, as seen by the high contrast phases, and the average length of the carbides was 10.6  $\mu\text{m}$ .

The as-levitation zone melted alloy structure is distinguished by four different regions as shown in Fig. 4a: the directionally solidified (DS), meltback, planar front growth (PG), and power down (PD) regions. The as-cast dendritic structure began to fade when the zone melting process started (DS), as evidenced by the gradual loss of the dendritic microstructure and loss of contrast variation corresponding to residual microsegregation between the DS and meltback regions. The dendritic structure was completely eliminated when a planar front started growing (PG), and this single crystal, microsegregation-free region was observed to be 3.6 mm long. During power down (PD), the dendritic structure began to reappear first in the form of a cellular microstructure (Fig. 4b). In this region, carbides precipitated at cell boundaries in the cellular structure and eventually in interdendritic regions. The density of carbides increased significantly as the microstructure transitioned from cellular to fine dendritic structure, and the density of solidification-induced porosity increased as the microstructure transitioned as well.

Cuboidal  $\gamma'$  precipitates were observed in the PG region as shown in Fig. 4c. The average edge length of  $\gamma'$  precipitates was 1.0  $\mu\text{m}$  and the  $\gamma'$  area fraction was 62.7%. This revealed  $\gamma'$  coarsening occurred due to a low cooling rate during the zone melting process. Grain boundaries, dendrites, and

microsegregation were not observed in the PG region. Porosity was also observed in PG region (0.072%); however, the area fraction was significantly lower compared to the DS region (0.24%), meltback (0.33%), and PD regions (2.96%). Since the existing porosity was not expected at the planar front, it is assumed it was created by the sectioning process by the electrical discharge machining.

The composition profile of the SHT specimen measured from EPMA is in good agreement with theoretical and model predictions obtained from the zone melting mass balance model integrated with Thermo-Calc, as shown in Fig. 5. A significant change of measured composition was observed in the transient meltback and PD regions, as exemplified by the decrease of Al content from 14.0 at.% to 12.0 at.% in the meltback region and increase of Al content from 12.1 at.% to 13.8 at.% in the PD region. Note that the PD region corresponds to the last liquid zone, and because the concentration profile was not measured for the complete PD region, the mass balance did not fully recover between DS and PD regions, as shown in Fig. 5.

In the PG region, the concentration of Al, Cr, and Ta increased steadily in the direction parallel to planar growth whereas Ni, Co, W, and Re concentrations decreased. These results indicate that Al, Cr, and Ta partition to the liquid and exhibit partition coefficients,  $k_i = C_S^i/C_L^i$  where  $C_S^i$  and  $C_L^i$  are compositions of the solid and liquid of the  $i$ th element, respectively, of less than unity, whereas Ni, Co, W and Re partitioned to solid and exhibit partition coefficients greater than unity. These results are mostly in agreement with the partitioning trends in CMSX-4 and PWA1484.<sup>18</sup> Partition coefficients were directly calculated via Thermo-Calc using the TCNI8 database for predicting the composition during the levitation zone melting process, as they can change with temperature and composition. The predicted partition coefficients are in good agreement with experimental results.

These experimentally measured compositions within the PG region are consistent with the thermodynamic modeling, which also predicted a monotonic change of composition of each alloying element as the planar front grew, as shown in Fig. 5. The measured composition and predicted composition of the PG region agree well; however, a noticeable difference in Cr and Ni content between the predicted and experimentally measured values was observed. The measured Cr and Ni compositions differed by 0.96% (Ni) and 0.60% (Cr) compared to the nominal alloy composition. The very gradual and monotonic change in the PG region solid composition shows that steady-state conditions were not achieved, such that the liquid would become saturated in solute and the alloy would solidify with a composition identical to the nominal alloy composition. For the given conditions, our model revealed that steady-state planar growth,

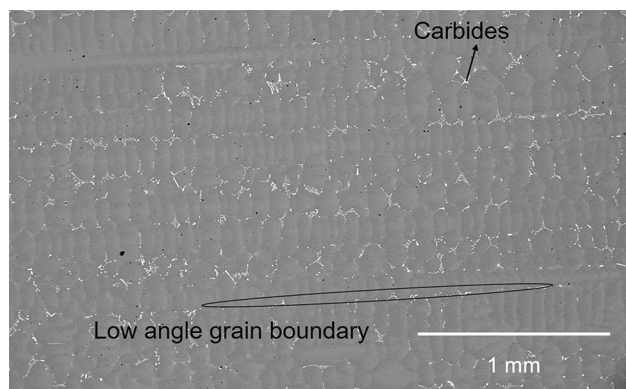


Fig. 3. SEM image of as-cast directionally solidified (DS) microstructure.

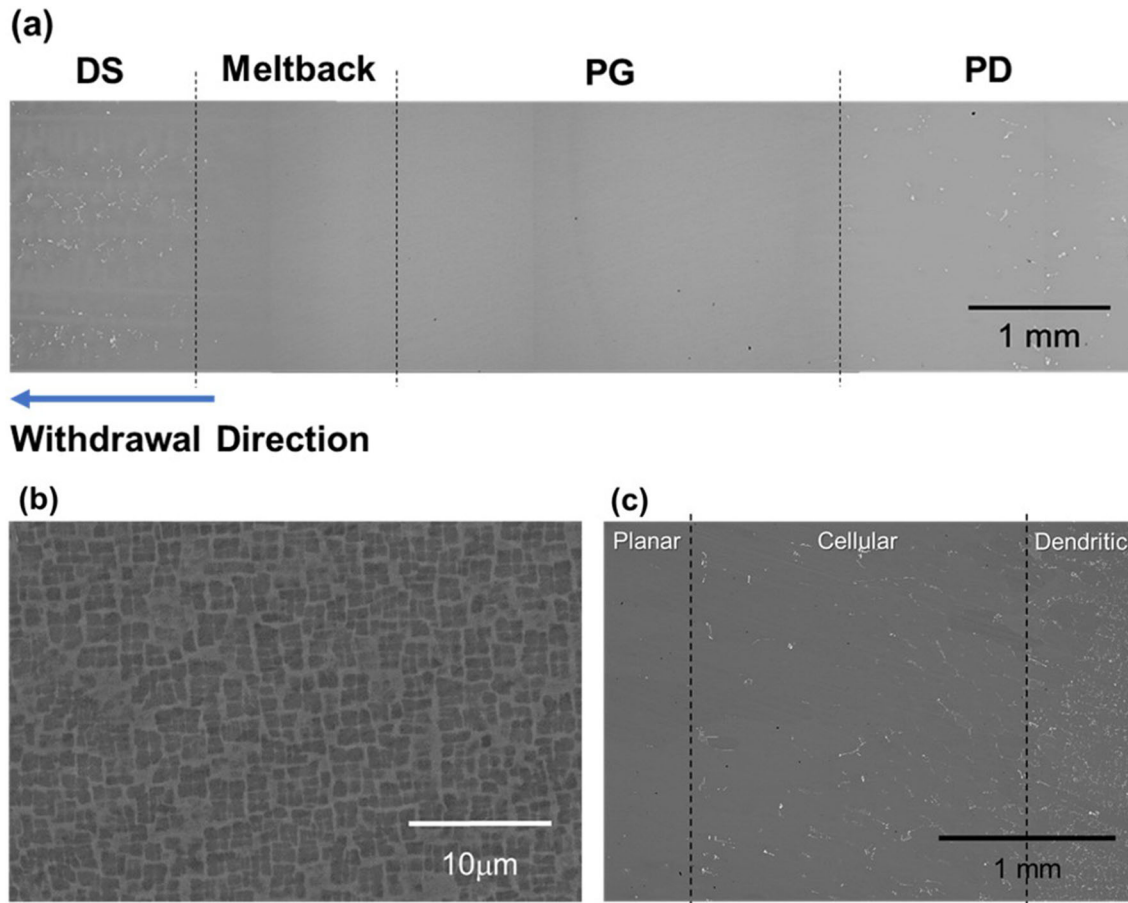


Fig. 4. (a) Overview of as-levitation zone melted of René N515, and (b) planar front—cellular structure transition during power-down, and (c) as-zone melted microstructure of PG region of René N515.

whereby the solid composition is within 5% of the nominal composition, would be achieved at a distance of 12.7 mm.

Hardness profiles across the as-levitation zone melted material were measured and the microstructure corresponding to the solidification region are shown in Fig. 6. The corresponding yield stress was estimated by:<sup>19</sup>

$$\sigma_y \approx H_V/3 \quad (3)$$

where  $H_V$  is the Vickers microhardness. The hardness varied minimally across the DS, meltback, and PG regions, but significantly decreased in PD region. Although the variance in the first three regions was relatively small in the DS, meltback, and PG regions, the overall measured hardness values were comparable. In these three regions, a decent area fraction of  $\gamma'$  precipitates in excess of 60% was observed.  $\gamma'$  coarsening occurred throughout DS, meltback, and PG regions, indicating diffusion-controlled  $\gamma'$  precipitation, and growth occurred with the transition of solid/liquid interface from DS, meltback, to PG region due to high temperature.<sup>20</sup> The average edge length of  $\gamma'$  precipitates was 1.02  $\mu\text{m}$  in the DS region, 1.99  $\mu\text{m}$  in the meltback

region, and 1.21  $\mu\text{m}$  in the PG region. Fine, irregular-shaped  $\gamma'$  precipitates were observed in the DS region. The  $\gamma'$  precipitate size increased, and the morphology changed from cuboidal to spherical in the meltback region. Finally, the precipitates exhibited a cube morphology in the PG region.<sup>21</sup> Large, eutectic-like  $\gamma'$  phase was observed in the DS and meltback regions whereas they were not observed in PG and PD regions, as shown in Fig. 6. Although carbides were observed near indentations in the DS and meltback regions, there was no correlation between the carbide formation and hardness in both trials. The shape of the indentation significantly changed in the PD region, and slip bands were observed emanating outwards from the edge of the indentation.

## DISCUSSION

The presence of a dendritic structure, microsegregation, and carbides in the directionally solidified material indicate inhomogeneity in composition and properties; the absence of these features in the PG material confirms that the PG region is homogeneous. This is also supported by a very low density of solidification porosity observed in this region. The

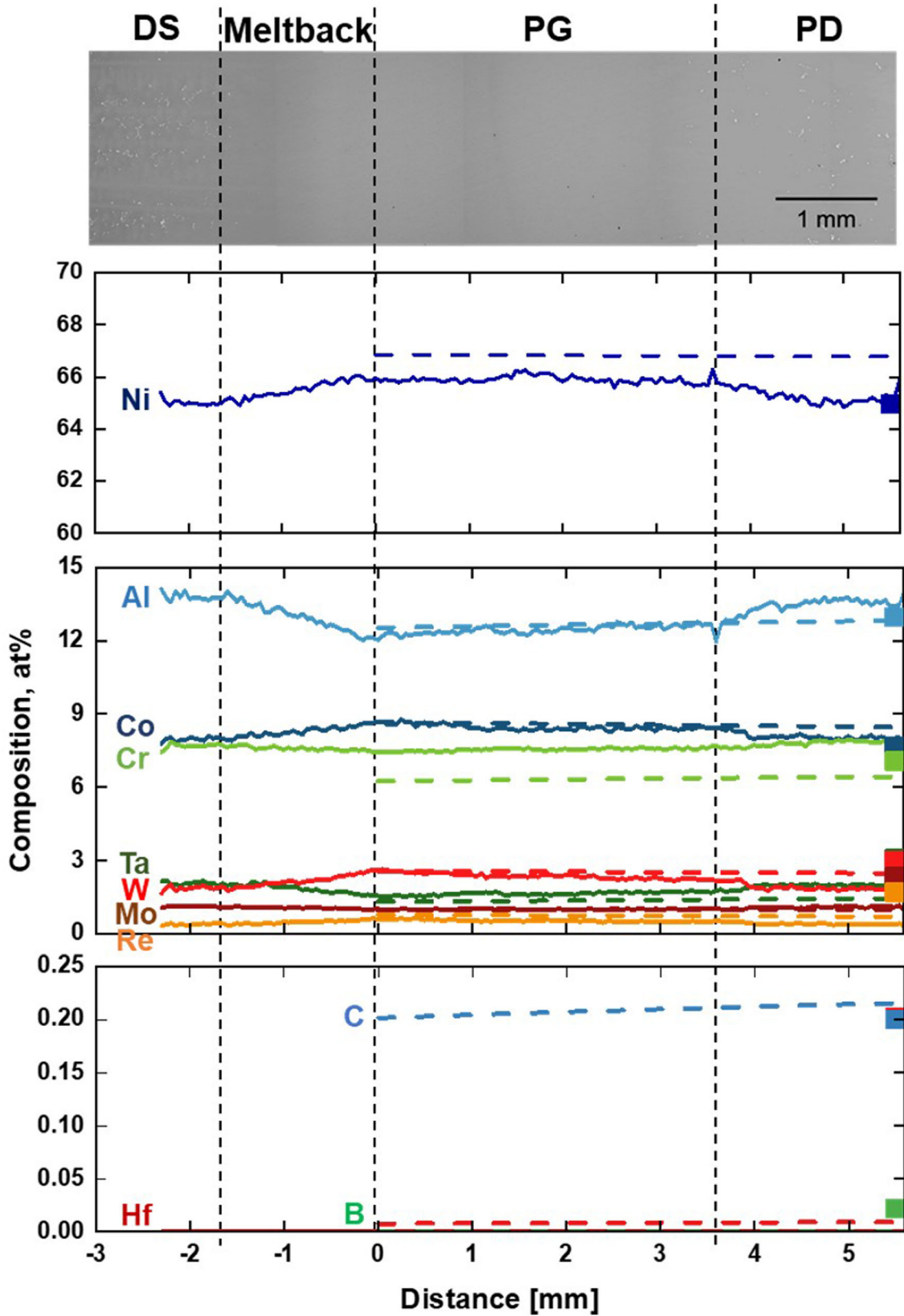


Fig. 5. Composition profile of the solution-annealed levitation zone melted René N515 as a function of position along the bar. The *solid line* represents EPMA measurement results, the *dotted line* represents thermodynamic concentration profile calculation for planar front growth region, and *square symbols* represent the nominal composition of René N515. One point in the DS regime was omitted because it measured the carbide composition.

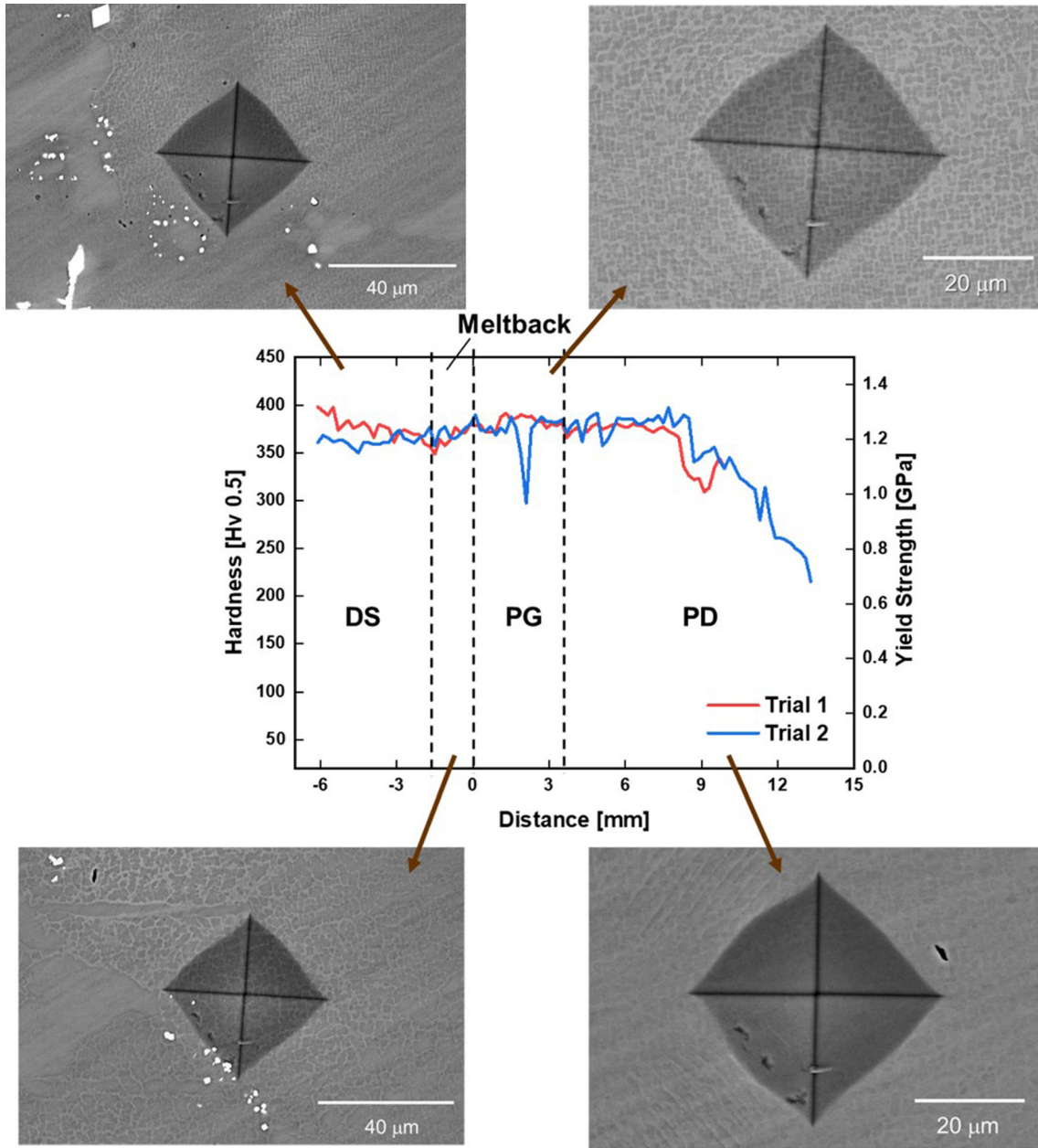


Fig. 6. Vickers hardness and estimated yield strength profile in the as-levitation zone melted specimen as a function of position along the bar. The yield stress was estimated by  $\sigma_y \approx H_V/3$ , and the microstructure near the indentation at each region.

successful construction of the homogeneous structure at the planar front is confirmed by the fact that there is no large, eutectic-like  $\gamma'$  phase in the PG region, as shown in Fig. 6, which is typically observed in dendritic structure as well.<sup>11</sup>

The composition gradients of all elements are nearly constant throughout the PG region, as shown in Fig. 5. However, a significant change in composition was observed in the DS, meltback, and PD regions due to transients in the melting and solidification behavior near these regions. Upon initial melting, the measured solid composition altered until a kink in the composition profile was observed at 0 mm. This kink should correspond with the start

of solidification at  $z = 0$  such that the composition of the solid is  $C_S^i = k_i C_L^i$ . The measured solid compositions at  $z = 0$  agree well with calculated values of the solid composition using measured alloy compositions from the DS region with measured partition coefficients in similar alloys from Ref.<sup>10</sup> For example, for measured Al and W compositions of 14.1 at.% and 2.2 at.%, the predicted initial solid compositions using partition coefficients of  $k_{Al} = 0.87$  and  $k_W = 1.42$  are 12.3 at.% and 3.1 at.% for Al and W, respectively. The predicted composition was calculated based on the nominal composition, whereas the measured composition at the PG region represents both directionally solidified and levitation

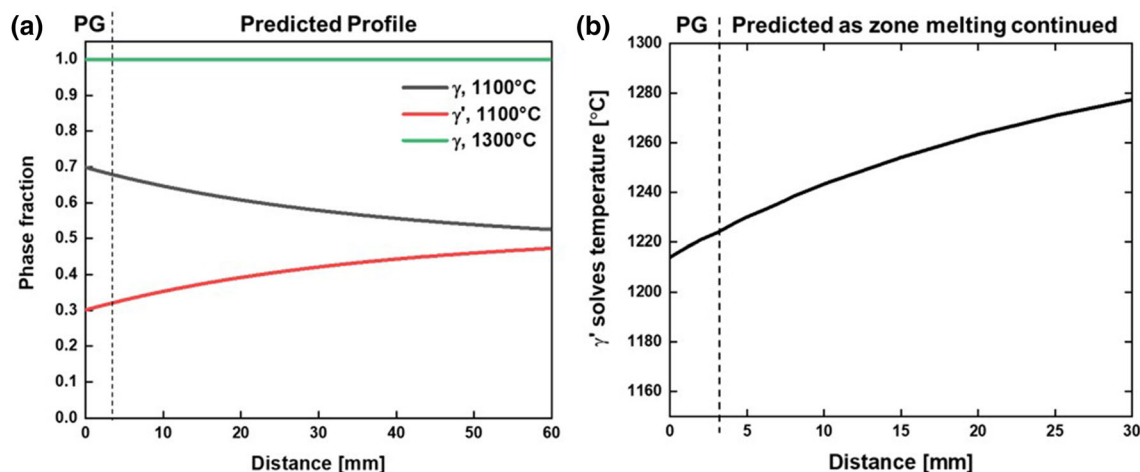


Fig. 7. (a) Predicted phase fraction at 1100°C and 1300°C of  $\gamma$  and  $\gamma'$  phase, and (b)  $\gamma'$  solvus temperature as a function of position along the bar (as levitation zone-melted). The phase fraction of planar front fabrication of this study was predicted from 0 mm to 3.6 mm, and the predicted phase fraction was kept calculating until the composition become the steady-state condition.  $\gamma'$  phase fraction is predicted to be 45% after the composition becomes steady-state.

zone melted compositions. This can cause a noticeable difference between the predicted and the measured composition. For instance, for Cr, the predicted value was lower than the nominal value, and the measured value at the PG region was lower than the DS region. This trend is consistent with the trend of Al and Ta which has a partition coefficient of  $k < 1$  in this alloy system. It is considered that Cr was almost uniformly distributed in the DS region with a higher content than nominal because of the directional solidification method, and was not significantly affected by levitation zone melting, which can transport solute to the liquid. A similar trend can be seen in Mo, which started with less content in the DS region due to the partition coefficient  $k > 1$ . Conversely, the subsequent excess or depletion of solute in the liquid should be observed near the end of the PD region. However, because solidification in the PD region occurred over a large length and the excess or depleted solute was distributed over this length, excess or depleted solute content was not observed in the EPMA measurements.

Significant changes to  $\gamma'$  morphology and  $\gamma'$  coarsening occurred throughout the DS, meltback, and PG regions due to the low cooling rate during the zone melting process. The  $\gamma'$  size generally increased from the DS to meltback region and again decreased in the PG region, as seen in Fig. 6. Furthermore, the area fraction of the large eutectic-like  $\gamma'$  phase was highest in the DS and meltback regions, likely due to larger cooling rates.<sup>10,22</sup> The  $\gamma'$  morphology transitioned from irregular cuboidal in the DS region, to irregular in the meltback, to irregular split in the PG region. The average edge length of  $\gamma'$  precipitates was 1.02  $\mu\text{m}$  in the DS region, 1.99  $\mu\text{m}$  in the meltback region, and 1.21  $\mu\text{m}$  in the PG region. The largest  $\gamma'$  precipitates were observed in the meltback region because pre-existing

precipitates experienced the longest time for coarsening throughout the levitation zone melting process (pre-heating + planar front fabrication). From the DS to meltback region, the eutectic  $\gamma'$  area fraction decreased from 18.5% to 10.2%. The eutectic  $\gamma'$  fraction decreased, whereas the as-cast  $\gamma'$  precipitates fraction increased as the dendritic structure disappeared and started to transition to the planar front structure. Since the dendritic arm spacing (DAS) gradually increased from DS to meltback, microsegregation decreased from the DS towards the meltback region with the decrease of eutectic  $\gamma'$  area fraction.<sup>20</sup>

The calculated phase fraction profiles at 1100°C, 1300°C, 1340°C is shown in Fig. 7a. The formation of  $\gamma'$  phase was only predicted at 1100°C, whereas the formation of the  $\gamma$  phase was predicted at all temperatures. This indicated that the  $\gamma'$  solvus temperature of this alloy was between 1100°C and 1300°C. The  $\gamma'$  solvus temperature was calculated based on the predicted composition along the bar. It was 1214°C at the beginning of the PG region, then rapidly increased to 1278°C as the planar front grew to 30 mm in the prediction, as shown in Fig. 7b. The predicted  $\gamma'$  phase fraction in the PG region was 30–33%, which is far less than the actual  $\gamma'$  area fraction. This indicates that significant  $\gamma'$  coarsening occurred below the  $\gamma'$  solvus temperature so that the  $\gamma'$  phase fraction increased significantly.<sup>20</sup> The  $\gamma'$  phase fraction slightly increased in the PG region and eventually became constant as zone melting continued, despite small changes to the alloy composition in the PG region. This is consistent with the experimentally obtained microstructure, where carbides did not exist in PG region but began to precipitate in the PD region between cells and dendrites, where a high concentration of solute could be found.



To achieve steady-state planar growth whereby the composition of the solidifying solid matches that of the nominal alloy composition, fabricating a longer planar front region is proposed. A longer planar front region can be achieved by increasing the solidification rate; however, the thermal gradient also needs to be significantly increased as shown in Fig. 1b. Experimentally, the solidification rate can be increased by decreasing the diameter of the initial directionally solidified bar in order to increase the thermal gradient significantly. In the real manufacturing process, maintaining a high thermal gradient uniformly throughout the process would be very challenging because of the relatively large size of components to fabricate.

The variance of the measured hardness is minimal across the DS, meltback, and PG regions. The relatively constant hardness values are likely due to the uniform distribution of  $\gamma'$  precipitates across these regions despite their morphological variances. The significant decrease in hardness observed in the PD region likely occurred due to the lack of coarse  $\gamma'$  precipitates in this region. The precipitates in the last parts of the PD region cannot be expected to exhibit comparable strength compared to the DS, meltback, and PG regions due to a lack of time to grow the  $\gamma'$  precipitates because the PD region cooled much more quickly than other regions.

Although there is minimum change in the hardness, the PG region would be expected to possess superior fatigue resistance and creep properties compared with a conventional directionally solidified material. Tien et al.<sup>23</sup> argued that a uniform distribution of  $\gamma'$  precipitates at the planar front would contribute to improving creep resistance significantly by improved phase stability. Also, past studies confirmed that crack initiation sites are usually due to casting porosity and carbides when fatigue tests were performed.<sup>6,7,10,11</sup> Since the density of porosity is relatively low and carbides are entirely eliminated in PG region, it is expected that this region is most likely to show superior creep and fatigue resistance.

## CONCLUSION

Analysis of microstructure, local composition, and mechanical properties of planar front Ni-based superalloys have suggested the possibility of eliminating microsegregation and casting defects which are two significant problems of the conventional directional solidification casting process. The following conclusions are drawn from this work:

1. A 3.6-mm-long, dendrite-free, carbide-free, and microsegregation-free planar front Ni-based superalloy was successfully fabricated by the levitation zone melting process.
2. The density of casting porosity was significantly decreased from 0.24% to 0.072% (area fraction)

in the planar front region.

3. A monotonic change of the composition in the planar front region was consistent with thermodynamic modeling predictions.
4. In the planar front region, Al, Cr, and Ta preferably partitioned to liquid, whereas Ni, Co, W, and Re preferably partitioned to solid.
5. Carbides only formed during the latter stages of power down, where rapid solidification, low thermal gradients, and microsegregation between cells and dendrites were observed.

## ACKNOWLEDGEMENTS

S.M and M.S.T. acknowledge support from the National Science Foundation (NSF CAREER DMR-1848128).

## REFERENCES

1. T.M. Pollock and S. Tin, *J. Propuls. Power.* 22, 361 (2006).
2. R.C. Reed, *The superalloys*, 1st ed. (New York: Cambridge University Press, 2006), pp. 19–20.
3. D.P. DeLuca and C.M. Biondo, U. S. Patent 5.820.700, 1998.
4. A.J. Wasson and G.E. Fuchs, *Superalloys 2008: Proceedings of 11th International Symposium on Superalloys* (2008).
5. T. Jin, W. Wang, X. Sun, and Z. Hu, *Mater. Sci. Forum* 638–642, 2257 (2010).
6. Q. Feng, L.J. Carroll, and T.M. Pollock, *Metall. Mater. Trans. A* 37, 1949 (2006).
7. J.D. Miller, PhD Thesis, University of Michigan, Ann Arbor, USA, 2011.
8. S. Huang, P.H. Monaghan, J. Zhao, and X. Gigliotti, U. S. Patent 6,127,286, 2001.
9. S. Tin and T.M. Pollock, *J. Mater. Sci.* 39, 7199 (2004).
10. S. Tin and T.M. Pollock, *Metall. Mater. Trans. A* 34, 20 (2003).
11. J.K. Tien and R.P. Gamble, *Mater. Sci. Eng.* 8, 152 (1971).
12. S. Steuer, P. Villechaise, T.M. Pollock, and J. Cormier, *Mater. Sci. Eng. A* 645, 109 (2015).
13. J.K. Tien, *Superalloys 1972: Proceedings of 2nd International Symposium on Superalloys* (1972).
14. R.D. Reviere, B.F. Oliver, and D.D. Bruns, *Mater. Manuf. Process.* (1989). <https://doi.org/10.1080/10426918908956275>.
15. K.E. Luitjohan, M.J.M. Krane, V. Ortalan, and D.R. Johnson, *J. Alloys Compd.* 732, 498 (2018).
16. K.E. Luitjohan, M.J.M. Krane, and D.R. Johnson, *ISIJ Int.* 60, 92 (2020).
17. D.R. Johnson, X.F. Chen, B.F. Oliver, R.D. Noebe, and J.D. Whittenberger, *Intermetallics* 3, 99 (1995).
18. R.A. Hobbs, S. Tin, and C.M.F. Rae, *Metall. Mater. Trans. A* 36, 2761 (2005).
19. L.E. Murr, E. Martinez, X.M. Pan, S.M. Gaytan, J.A. Castro, and C.A. Terrzas, *Acta Mater.* 61, 4289 (2013).
20. X. Guo, H. Fu, and J. Sun, *Metall. Mater. Trans. A* 28, 997 (1997).
21. R.A. Ricks, A.J. Porter, and R.C. Ecob, *Acta Metall. Mater.* 31, 43 (1983).
22. J.J. Montoya-Cruz, R. Kadalbal, T.Z. Kattamis, and A.F. Giamei, *Metall. Trans. A* 13, 1153 (1982).
23. J.K. Tien and R.P. Gamble, U. S. Patent 3,677,835, 1972.
24. R.A. Abas, M. Hayashi, and S. Seetharaman, *Int. J. Thermophys.* 28, 109 (2007).

**Publisher's Note** Springer Nature remains neutral with regard to jurisdictional claims in published maps and institutional affiliations.